

A Two-Layer Electrostatic Film Actuator with High Actuation Stress and Integrated Brake

Huacen Wang, and Hongqiang Wang, *Member, IEEE*,

Abstract—Robotic systems driven by conventional motors often suffer from challenges such as large mass, complex control algorithms, and the need for additional braking mechanisms, which limit their applications in lightweight and compact robotic platforms. Electrostatic film actuators offer several advantages, including thinness, flexibility, lightweight construction, and high open-loop positioning accuracy. However, the actuation stress exhibited by conventional actuators in air still needs improvement, particularly for the widely used three-phase electrode design. To enhance the output performance of actuators, this paper presents a two-layer electrostatic film actuator with an integrated brake. By alternately distributing electrodes on both the top and bottom layers, a smaller effective electrode pitch is achieved under the same fabrication constraints, resulting in an actuation stress of approximately 241 N/m^2 , representing a 90.5% improvement over previous three-phase actuators operating in air. Furthermore, its integrated electrostatic adhesion mechanism enables load retention under braking mode. Several demonstrations, including a tug-of-war between a conventional single-layer actuator and the proposed two-layer actuator, a payload operation, a one-degree-of-freedom robotic arm, and a dual-mode gripper, were conducted to validate the actuator's advantageous capabilities in both actuation and braking modes.

I. INTRODUCTION

With the development of industrial automation and intelligent manufacturing technologies, the demand for robotic systems in human society has been steadily increasing. However, most robotic systems are based on magnetic motors combined with rigid transmission mechanisms, resulting in substantial mass [1]–[3] and limiting their applications in human-machine interaction and miniature robotics. Furthermore, to withstand static loads while maintaining a desired position, magnetic motors typically require external braking components [4]–[6] or closed-loop control systems [7]–[9], increasing the system complexity. Soft actuators, such as dielectric elastomers [10], [11], shape memory alloys [12], [13], and pneumatic actuators [14]–[16], have been widely applied in miniature robots, wearable devices, and grippers in recent years. However, their viscoelastic materials mostly result in limited accuracy and a long response time [17], [18].

Electrostatic film actuators (EFAs), driven by electrostatic forces generated between microscale comb electrodes embedded within the polymer film insulation [19], [20], offer advan-

This work was supported in part by the Natural Science Foundation of China under Grant 52275021 and 52450323, the Natural Science Foundation of Guangdong Province of China under Grant 2024A1515010183, and in part by Guangdong Provincial Research Support Program 2019QN01Z733. (Corresponding author: Hongqiang Wang.)

Huacen Wang is with the Department of Mechanical and Energy Engineering, Southern University of Science and Technology, Shenzhen 518055, China.

Hongqiang Wang is with the Department of Mechanical and Energy Engineering, Southern University of Science and Technology, Shenzhen 518055, China (e-mail: wanghq6@sustech.edu.cn).

tages including thinness, flexibility, lightweight construction, and high open-loop positioning accuracy. In addition, they can provide sufficient actuation velocity and force [21], making them suitable for applications in human-machine interaction [22], [23] and bio-inspired robotics [24]–[26]. Due to their operation under high driving voltage amplitude but relatively low current, EFAs also exhibit resistance to strong magnetic interference [27], [28].

However, in conventional flexible printed circuit manufacturing processes, both the electrode width and spacing are constrained by the same minimum feature size. Conventional EFAs arrange all electrodes within a single electrode layer [29]–[31], limiting further reduction of effective electrode pitch (the sum of the width and spacing) and thus restricting the achievable actuation force [32]. Moreover, the asymmetry in the distance between the electrode layer and the surfaces results in unbalanced actuation forces on both sides of the film, which degrades performance when multiple layers are stacked [20], [33]. A four-phase two-layer EFA design has previously been reported to achieve higher actuation stress and applied to mesoscale artificial muscles [32]. However, it requires more precise fabrication techniques and more driving equipment. Accordingly, the development of electrode design capable of enhancing the actuation force density within the constraints of existing fabrication processes remains a challenge in advancing EFA performance.

The contributions of this work are as follows. In this work, we propose a two-layer EFA (Fig. 1a), where electrodes are alternately arranged more densely across the upper and lower layers. This design enables a smaller effective electrode pitch under the same fabrication conditions, resulting in higher actuation stress compared to conventional three-phase EFAs under the same driving voltage amplitude, as shown in Fig. 1b. In addition, the larger spacing between electrodes in the same layer improves the breakdown strength compared to the four-phase EFA, achieving actuation stresses up to approximately 241 N/m^2 and allowing the actuator to operate with a payload of approximately 68.2 times its own weight. Benefiting from the symmetric two-layer electrode design, the actuation film generates equal output forces on both sides, thereby facilitating force enhancement through stacking multiple films. Furthermore, the electrode coverage ratio reaches as high as 83.3% (with half of the electrodes located on the other layer), enabling the actuator to generate up to 12.0 N of electrostatic adhesion force for braking functionality. Based on this two-layer EFA with integrated brake, we demonstrate its application in driving a one-degree-of-freedom (DOF) robotic arm capable of handling heavier loads during active braking. Moreover, a dual-mode gripper is developed, utilizing the EFA's actuation mode for object grasping and its braking mode

for object holding.

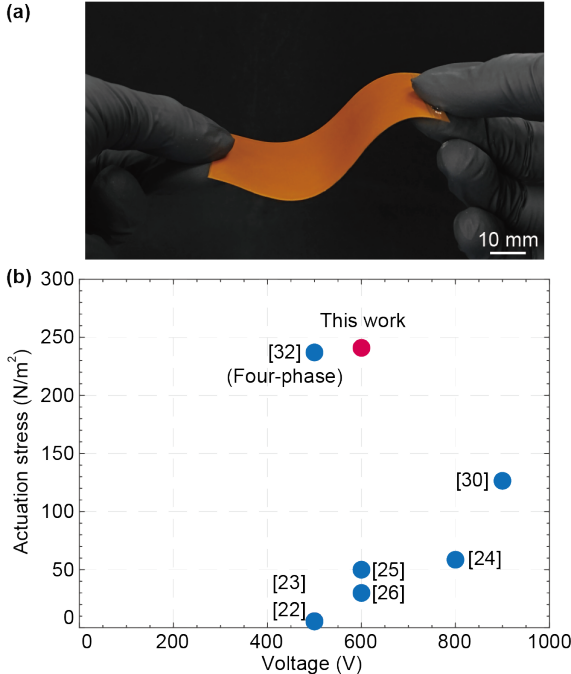


Fig. 1. The two-layer electrostatic film actuator. (a) Demonstration of the flexible and thin structure of the actuator. (b) Comparison of the actuation stress of the proposed two-layer three-phase actuator with previously reported actuators operating in air.

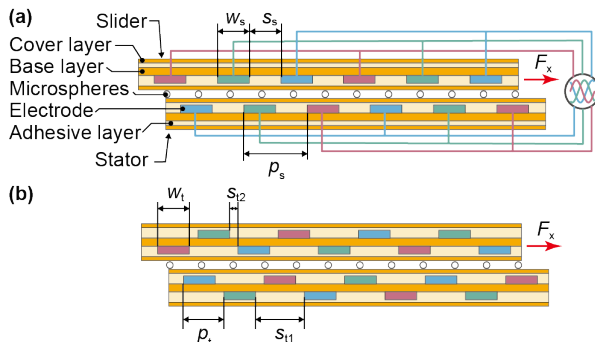


Fig. 2. The principle and design of (a) conventional single-layer EFA and (b) the two-layer EFA.

The structure of this paper is organized as follows. Section II presents the working principle and design of the two-layer EFA. Section III describes the fabrication process and the microstructure of the actuator electrode. Section IV details the experimental setups and evaluates the actuator's performance. Section V demonstrates the applications of a robotic arm and a gripper. Section VI concludes the paper and discusses future work.

II. ACTUATOR DESIGN AND ANALYSES

A. Principle and design of the two-layer EFA

The design of the slider and stator in conventional single-layer EFAs is shown in Fig. 2a. Three-phase electrodes are arranged in parallel on the base layer and electrically insulated by the cover layers through adhesive layers. In terms of electrode parameters, w_s denotes the electrode width, s_s

represents the electrode spacing, and p_s , defined as the sum of the width and spacing ($p_s = w_s + s_s$), is referred to as the effective electrode pitch. Due to the identical minimum size limitation of the fabrication process for both width and spacing, w_s is typically designed to be equal to s_s . As a normal adhesion force is generated between the slider and the stator during operation, glass beads (with a diameter of 20 to 30 μm) are uniformly applied to the contact surfaces of the films to reduce friction. When three-phase sinusoidal voltages with initial phase differences of 120° are applied to the electrodes, a horizontal driving force F_x is generated on the slider, which can be expressed as [21]:

$$F_x = K_a v_a^2 \sin(\theta_e - 2\phi), \quad (1)$$

where $K_a = k_a A_e$ is the actuation force constant with units of $\text{N}\cdot\text{V}^{-2}$ of the actuator. k_a is a material-dependent force coefficient with units of $\text{N}\cdot\text{m}^{-2}\cdot\text{V}^{-2}$. A_e is the effective actuation area of the actuator. v_a is the amplitude of the driving voltages. $\theta_e = 2\pi x_{\text{sl}}/3p$ represents the electric angle of the slider position x_{sl} along the X direction, with p denoting the effective pitch. The parameter ϕ is the excitation phase of the applied voltage.

Since EFAs operate in synchronous motion, their actuation velocity can be expressed as [34]:

$$v = 6pf, \quad (2)$$

where f is the driving frequency of the applied voltage.

The design of the proposed two-layer EFA is illustrated in Fig. 2b. The electrodes are alternately arranged on both the top and bottom layers. In this configuration, s_{t1} denotes the electrode spacing on the same layer, s_{t2} represents the adjacent electrode spacing on different layers, and the effective electrode pitch $p_t = w_t + s_{t2}$. When utilizing an identical fabrication process for both single-layer and two-layer designs, the electrode widths remain the same ($w_t = w_s$). Since s_{t2} can be adjusted without requiring higher fabrication precision, a smaller effective pitch can be achieved when s_{t2} is between 0 and s_s , resulting in p_t smaller than p_s . Meanwhile, the same-layer electrode spacing satisfies $s_{t1} = w_t + 2s_{t2}$, which is larger than s_s ($s_s = w_t = w_s$), resulting in a higher breakdown strength and thus enabling a higher maximum actuation force of the EFA.

In addition to actuation, the electrostatic adhesion capability of the two-layer EFA can be utilized for braking. During adhesion operation, all slider electrodes are connected to a square-wave AC voltage, while all stator electrodes are grounded. Under this configuration, the system can be approximated by a parallel-plate capacitor model, and the normal adhesion force can be calculated as [35]:

$$F_n = K_b v_b^2, \quad (3)$$

where K_b is the adhesion force constant with units of $\text{N}\cdot\text{V}^{-2}$ based on the materials and dimensions of the electrostatic adhesive pad, v_b is the amplitude of the driving voltage for adhesion. Since the actuation force operates tangentially, the corresponding tangential adhesion force used for braking can be expressed as:

$$F_t = \mu_b F_n = \mu_b K_b v_b^2, \quad (4)$$

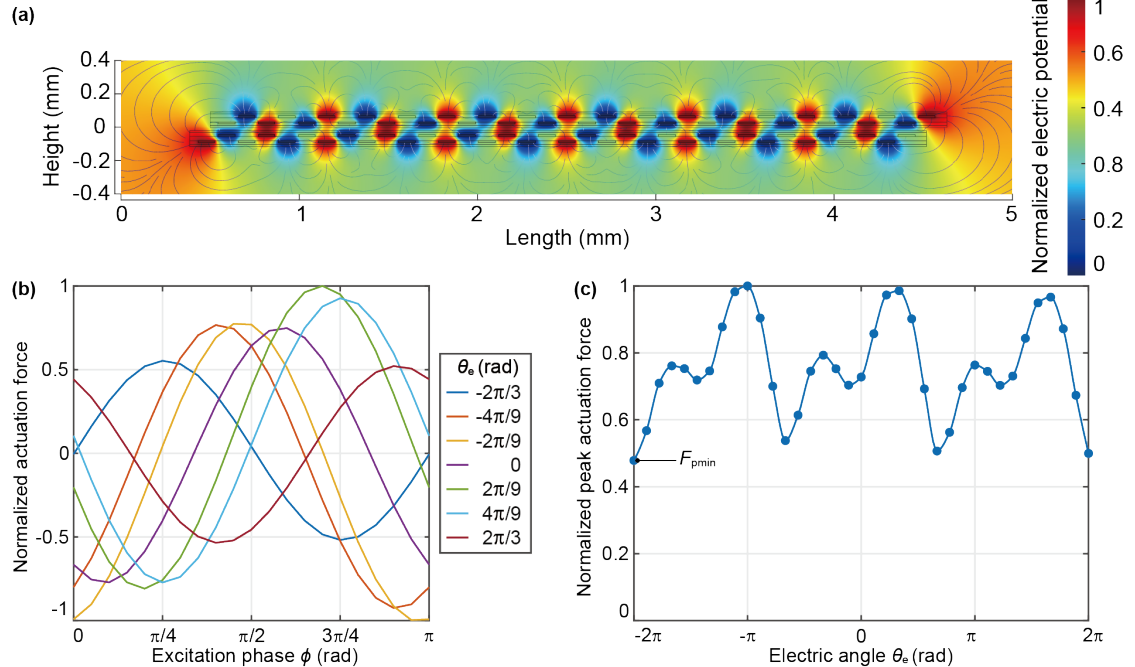


Fig. 3. Analysis of the two-layer EFA. (a) The normalized electric potential distribution of Actuator 1. (b) Relationship between normalized actuation force and excitation phase in different electric angles. (c) Relationship between normalized peak actuation force and electric angle.

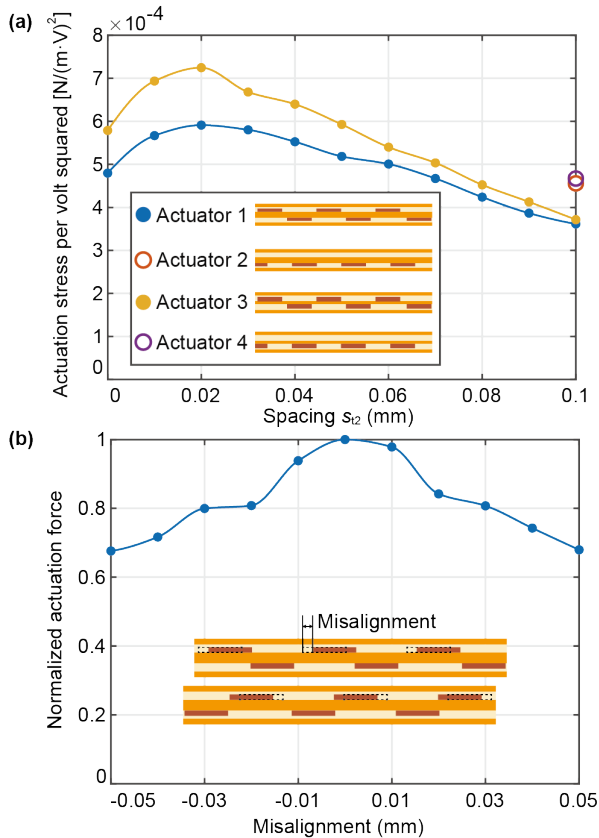


Fig. 4. The influence of design and fabrication parameters on the actuation force. (a) Relationship between actuation stress per volt squared and spacing. (b) Relation between normalized actuation force and misalignment.

where μ_b is the friction coefficient between the slider and the stator.

B. Finite element analysis

Finite element analysis was employed to investigate the effects of electrode configurations and fabrication parameters on the actuation forces of EFAs. In the simulation, the slider and stator were positioned inside an air-filled enclosure, with an air gap of $20 \mu\text{m}$ and a relative permittivity of 1. The base layer and cover layer materials were set as polyimide with a relative permittivity of 3.4, while the adhesive layer was set as acrylic adhesive with a relative permittivity of 3.5. The electrode material was set as copper. The thicknesses of the cover layer and adhesive layer were set to $13 \mu\text{m}$ and $2 \mu\text{m}$, respectively. As summarized in Table I, simulations were carried out for four types of actuators to compare their actuation forces under different design parameters. Specifically, combinations of electrode layer thickness and base layer thickness were selected based on two kinds of commercially available double-sided copper-clad laminates.

TABLE I
THE PARAMETERS OF FOUR TYPES OF ACTUATORS IN SIMULATIONS.

Actuator	Single/two-layer	Thickness (μm)	
		Electrode layer	Base layer
Actuator 1	Two	12	25
Actuator 2	Single	12	25
Actuator 3	Two	18	12.5
Actuator 4	Single	18	12.5

By applying driving voltages to the electrodes of each phase in the simulation, as shown in Fig. 3a, the electric potential distribution of the two-layer EFA (corresponding to Actuator 1 in Table 1, with $w_t = 100 \mu\text{m}$ and $s_{12} = 20 \mu\text{m}$) was obtained. This further yielded the relationship between the normalized actuation force and the excitation phase at different electric angles within two effective pitches (the period of the two-layer actuator spans six effective pitches), as shown in

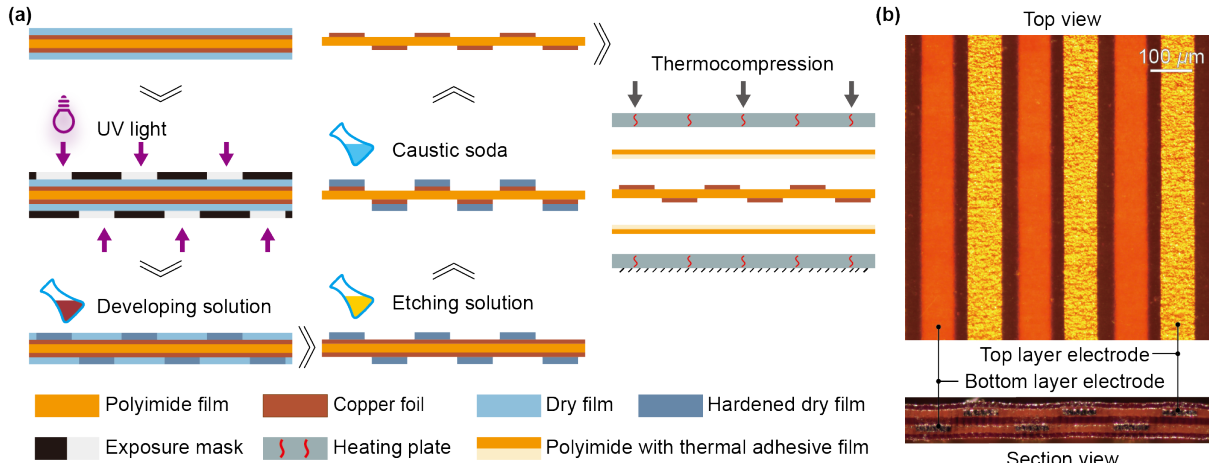


Fig. 5. Fabrication of the two-layer actuator. (a) The illustration of the fabrication process. (b) The top and sectional views of the electrodes.

Fig. 3b. The relationship between the peak actuation force and electric angle is presented in Fig. 3c, where $F_{p\min}$ denotes the maximum achievable normalized actuation force during continuous motion.

To identify optimal design parameters for the two-layer EFA, the influence of the spacing s_{t2} on actuation force was further investigated. In this comparison, all electrode widths were fixed at 100 μm . For the single-layer EFAs (Actuators 2 and 4), the electrode spacing s_s was set to 100 μm . The relationship between actuation stress per volt squared and spacing s_{t2} is shown in Fig. 4a. The two-layer EFAs exhibited maximum actuation forces when s_{t2} was set to 20 μm , and were much higher than those of the single-layer counterparts (the force of Actuator 1 is 29.7% larger than that of Actuator 2).

In the fabrication process of the two-layer EFA, electrode misalignment between electrodes in the top and bottom layers may occur due to processing error. The influence of the misalignment on the actuation force was analyzed through simulation. The relationship between normalized actuation force and electrode misalignment is shown in Fig. 4b (corresponding to Actuator 1 with $w_t = 100 \mu\text{m}$ and $s_{t2} = 20 \mu\text{m}$). As the value of misalignment increases, the actuation force decreases significantly. Therefore, the misalignment should be controlled within 10 μm during fabrication to ensure optimal actuator performance.

III. FABRICATION

The fabrication procedure of the two-layer EFA film is shown in Fig. 5a. Firstly, a double-sided copper-clad laminate (comprising a 25 μm polyimide base layer and two 12 μm copper layers) served as the substrate for the actuator. Then, negative-type dry films were laminated to both sides of the substrate. Ultraviolet (UV) light was subsequently projected through exposure masks containing the designed electrode layouts. The exposed portions of the photosensitive dry films were hardened, forming insoluble resist layers, while the unexposed regions were removed by a developing solution (1% Na_2CO_3). The uncovered copper was then etched away using an etching solution (CuCl_2 and HCl), leaving the designed electrode patterns. After etching, the residual hardened dry

films were stripped with a caustic soda solution (3% NaOH), exposing the patterned flexible circuits. For insulation, two overlays (consisting of a 13 μm polyimide layer and a 13 μm thermal adhesive layer) were laminated onto both sides of the etched substrate using a thermocompression at 185°C and 2.3 MPa for 3 hours.

The final fabricated two-layer EFA film measured 100 mm \times 50 mm in length and width, with a total thickness of 90 μm and a mass of 0.88 g. The effective electrode area was 92.8 mm \times 45.6 mm. The microscopic top view and the section view of the fabricated electrodes are shown in Fig. 5b. Inside the actuation film, the electrodes were alternately distributed on the top and bottom layers. The fabricated copper electrodes had an average width of approximately 85 μm and a spacing of approximately 35 μm . These dimensions slightly deviate from the design values of 100 μm width and 20 μm spacing, which may be attributed to over-etching during the fabrication process.

IV. EXPERIMENT RESULTS

We experimentally explored the velocity, positioning accuracy, actuation force, and braking force of the two-layer EFA. In these experiments, control signals were generated by a controller board (SCB-68A, National Instruments) and amplified 1000 times using three high-voltage amplifiers (Model 615-3, Trek) to drive the actuator. Sensor data were collected using analog signal acquisition boards (TB-4309 and TB-4330, National Instruments).

A. Results of velocity and positioning accuracy

In the displacement measurement setup shown in Fig. 6a, the stator was fixed on an acrylic plate, while a reflector was mounted on the slider for displacement sensing via a laser displacement sensor (HG-C1200, Panasonic). In the displacement tests, the voltage amplitude was set to 500 V_{0-p}. The displacements of the actuator under different driving frequencies are presented in Fig. 6a. As shown in Fig. 6b, the actuator velocity exhibited a linear relationship with the driving frequency, which is consistent with the theoretical model. The maximum velocity reached approximately 167 mm/s at a 240 Hz driving frequency. To evaluate linear positioning

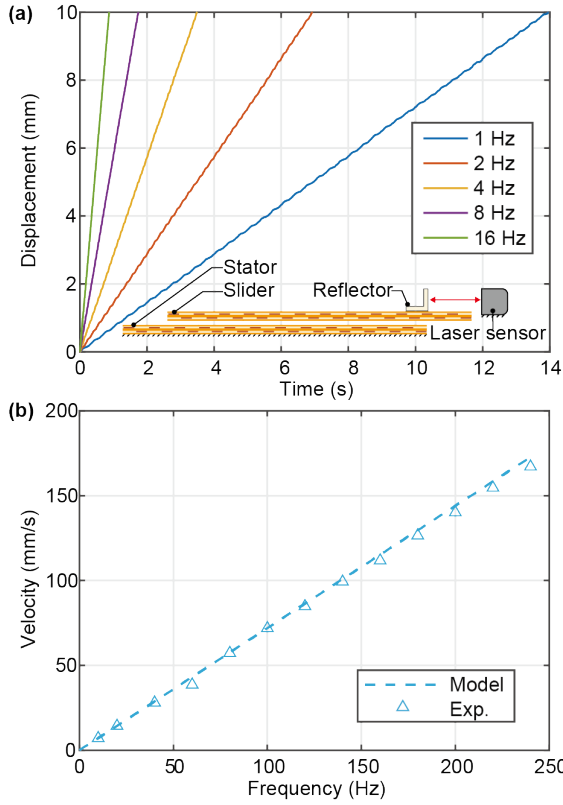


Fig. 6. The velocity of the actuator. (a) Schematic of the experimental setup and results of displacements in different driving frequencies. (b) Results of velocity in driving frequencies.

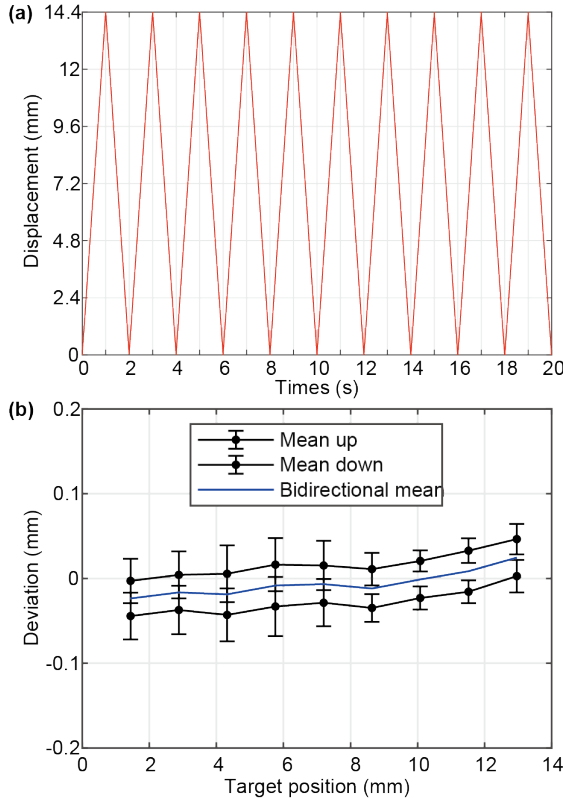


Fig. 7. The positioning accuracy of the actuator. (a) Results of displacement data for 10 cycles of reciprocal movements. (b) Results of the positioning error.

accuracy, the slider was driven to reciprocate over a 14.4 mm stroke at a driving frequency of 20 Hz for ten cycles, as shown in Fig. 7a. According to the results and based on the accuracy evaluation method of the Physik Instrumente (PI) [36], the mean bidirectional positioning accuracy of the actuator was 0.048 mm, with a bidirectional repeatability accuracy of 0.035 mm as shown in Fig. 7b.

B. Results of the actuation force

In the actuation force measurement setup shown in Fig. 8a, the stator was fixed on a 3D-printed sliding rail through screws. The slider was connected to a force sensor (LSB 201, FUTEK) via a hook and a spring. During the test, the actuator was applied with sinusoidal voltages with a 10 Hz driving frequency. As the slider stretched the spring leftward, the force sensor recorded the increasing force in real-time. The maximum force value was recorded as the actuation force since the slider could no longer extend the spring at a given voltage amplitude. The relationship between actuation force and voltage amplitude is shown in Fig. 8a, which is in agreement with the finite element model. A maximum actuation force of 1.02 N (corresponding to an actuation stress of approximately 241 N/m²) was achieved at 600 V_{0-p} voltage amplitude.

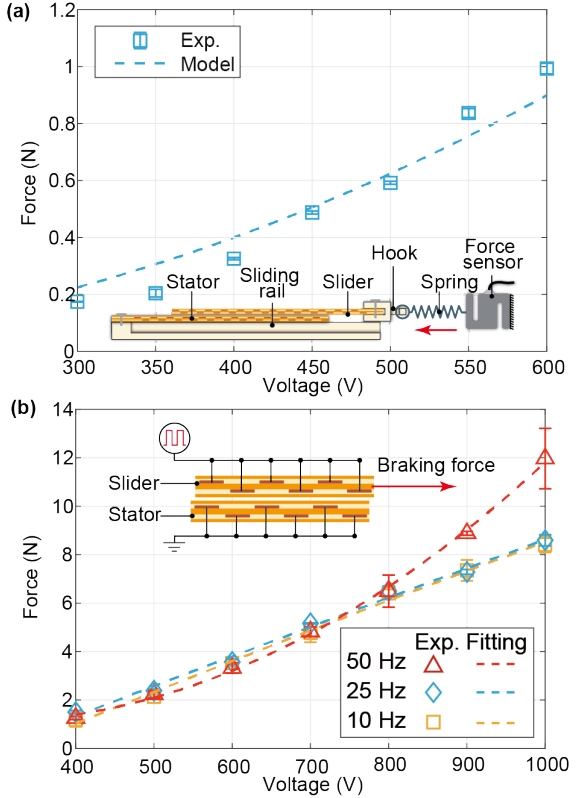


Fig. 8. The actuation force and braking force of the actuator. (a) Schematic of the experimental setup and results of the actuation force for different voltage amplitudes. (b) Results of the braking force for different voltage amplitudes and driving frequencies.

C. Results of braking force

The experimental setup for evaluating the electrostatic adhesion braking force is shown in Fig. 8b. The slider was

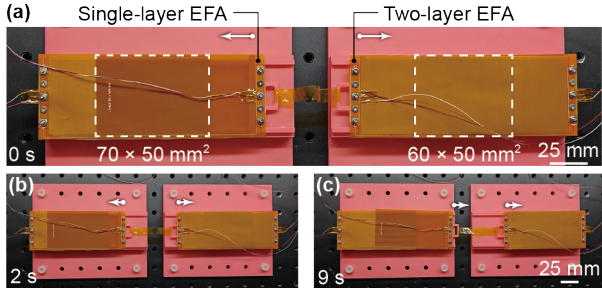


Fig. 9. The demonstrations of a tug-of-war between a single-layer EFA and the proposed two-layer EFA. (a) Initial state: the single-layer actuator with a larger initial effective area. (b) The tape is tighten as the two actuators start to compete. (c) The two-layer actuator eventually pulls the single-layer actuator away.

connected to a force sensor (LSB203, MTS) and moved at a constant velocity of 50 mm/min by a tensile test platform (Model 42, MTS). During testing, all electrodes on the slider were connected to a bipolar square-wave AC voltage, while the stator electrodes were grounded. The relationships between braking force and voltage amplitude under different driving frequencies are shown in Fig. 8b. The results indicate that the braking forces at 10 Hz and 25 Hz were similar; however, at 50 Hz, the braking force increased significantly at high voltage amplitude, reaching a maximum value of approximately 12.0 N at ± 1000 V. It is noteworthy that repeated vertical tensile tests may cause glass beads to detach from between the two films, increasing the friction coefficient. Therefore, the braking force measured in the tensile tests may be higher than that achievable under normal operating conditions.

V. DEMONSTRATIONS

A. Tug-of-war

To visually compare the actuation forces between conventional single-layer EFA and the two-layer EFA, a tug-of-war platform was designed as shown in Fig. 9 and Movie. On the left side, a single-layer actuator with an initial effective area of $70 \times 50 \text{ mm}^2$ was placed, while a two-layer actuator with an initial effective area of $60 \times 50 \text{ mm}^2$ was positioned on the right side. The sliders of both actuators were connected via a polyimide tape. Both actuators were simultaneously driven by sinusoidal voltages at 500 V_{0-p} amplitude and 5 Hz driving frequency.

At the beginning of the competition, the tape remained slack. After approximately 2 seconds, the tape was pulled taut, and both actuators began exerting opposing forces. Then, the single-layer actuator was pulled off-axis and lost the competition. By 9 seconds, the two-layer actuator had dragged the single-layer actuator out.

B. Payload operation

To evaluate the payload capability of the two-layer EFA, a testing platform was constructed as shown in Fig. 10. The stator was mounted on a sliding rail, while the slider was placed on top of the stator. When driven by sinusoidal voltages at 500 V_{0-p} amplitude and 30 Hz driving frequency, the slider performed a reciprocating motion, as shown in Fig. 10a and Movie for the unloaded case.

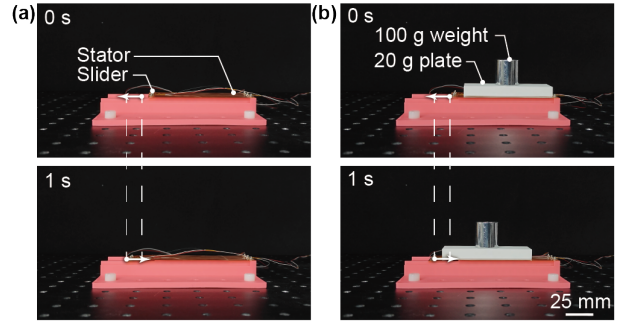


Fig. 10. The demonstrations of the payload capacity of the actuator. The slider of the actuator operates (a) no-load and (b) with a payload of approximately 68.18 times its own weight.

Subsequently, a 3D-printed plate (20 g) and an additional mass (100 g) were placed atop the slider, resulting in a total payload equivalent to approximately 68.2 times the actuator's own weight. As shown in Fig. 10b, the actuator maintained its full stroke without observable degradation in motion performance under this loading condition.

C. One-DOF robotic arm

To demonstrate the integrated braking capability of the two-layer EFA, the actuator was implemented as both the actuation and braking mechanism for a one-DOF robotic arm. Benefiting from the force superposition capability of the two-layer design, the actuator was constructed using three stator films and two slider films. The stator was mounted on the upper arm, while the slider was connected to the forearm via a thin cable. The actuator was driven by voltages at 500 V_{0-p} voltage amplitude and 5 Hz driving frequency.

As shown in Fig. 11a and Movie, the actuator successfully drove the robot arm in elbow-like rotational motion under unloaded conditions. The arm was also able to lift a plastic cup with a mass of 11.2 g from a lower initial angle, as illustrated in Fig. 11b. To further evaluate the payload limit during dynamic motion, water was incrementally added into the cup during operation. As shown in Fig. 11c, when the added water mass exceeded approximately 20 g at 1.5 seconds, the actuation force was no longer sufficient to maintain motion, resulting in slipping backward and ultimately causing the cup to tip over at 0.5 seconds.

After reaching the target position by actuation mode, the actuator was switched to braking mode by applying a ± 1000 V square-wave voltage at 50 Hz to the slider electrodes while grounding the stator electrodes. Under braking mode, as shown in Fig. 11d, the actuator was able to hold the arm position even when the payload exceeded 60 g at 7 seconds, preventing tipping and maintaining stability.

D. Dual-mode gripper

Based on two one-DOF robot arms, a dual-mode gripper was constructed by modifying the end-effector structures and assembling them into a gripping mechanism, as illustrated in Fig. 12 and Movie. The gripper successfully grasped a polyimide tape weighing approximately 20 g. During the grasping process, both actuators operated in actuation mode (500 V_{0-p} voltage amplitude with 5 Hz driving frequency) to

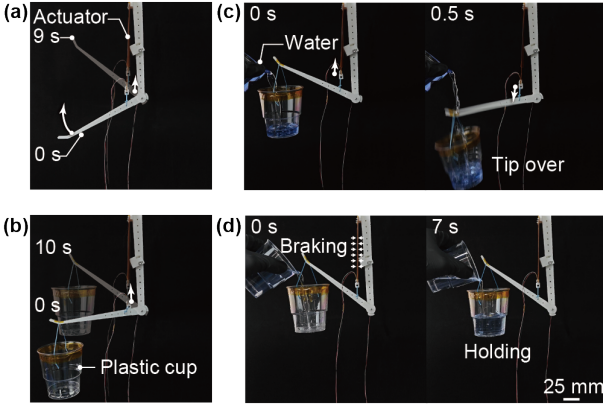


Fig. 11. The demonstrations of the actuator for a one-DOF robotic arm. The robotic arm lifts (a) no-load or (b) with a plastic cup. (c) The actuator slips backward when the water exceeds 20 g, causing the cup to tip over. (d) The actuator switches to the braking mode at the target position and is able to hold water exceeding 60 g.

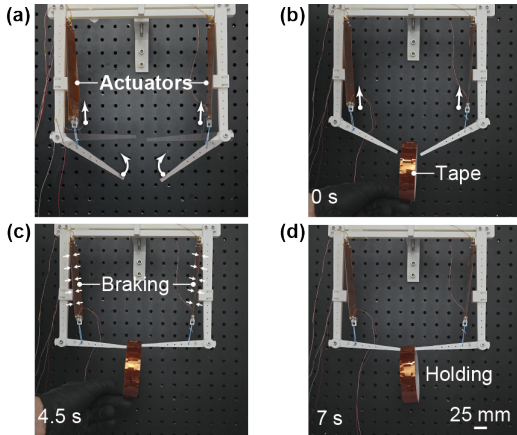


Fig. 12. A dual-mode gripper performs object grasping through the actuation mode of the actuator, and holds the object after closure using the braking mode.

drive the gripper fingers inward, allowing insertion into the hollow center of the tape. After approximately 4.5 seconds, once the gripper fully closed, the actuators were switched to braking mode (applying ± 1000 V square-wave voltage at 50 Hz to the slider electrodes while grounding the stator electrodes), thereby holding the grasped object.

VI. CONCLUSIONS

In summary, a two-layer EFA with integrated braking capability was proposed and experimentally demonstrated to address the force limitations of conventional EFAs operating in air. The two-layer electrode design enables a smaller effective electrode pitch without requiring higher fabrication precision, thereby significantly enhancing the actuation stress. Finite element simulations were conducted to analyze the effects of design parameters and fabrication misalignment on actuator performance. Experimental results confirmed that the proposed actuator achieved high actuation stress, precise positioning, and substantial payload capacity. A series of demonstrations, including tug-of-war, payload operation, robotic arm manipulation, and dual-mode gripping, further validated its applicability in both actuation and braking modes. Currently, the integrated braking mechanism is affected by the glass beads

during operation, which may significantly reduce the braking force. Future improvements may involve encapsulation of the actuator in a dielectric liquid to ensure stable braking performance. Additionally, the present fabrication process employs a relatively thick base layer, which could be further optimized to enable the two-layer design to achieve even higher actuation stresses. This two-layer EFA provides a promising solution for lightweight robotic systems that require compact, precise actuation combined with integrated braking functionality.

REFERENCES

- [1] D. Axinte, J. Allen, R. Anderson, I. Dane, L. Uriarte, and A. Olara, “Free-leg hexapod: A novel approach of using parallel kinematic platforms for developing miniature machine tools for special purpose operations,” *CIRP annals*, vol. 60, no. 1, pp. 395–398, 2011.
- [2] J. Liu, Y. Tian, and F. Gao, “A novel six-legged walking machine tool for in-situ operations,” *Frontiers of Mechanical Engineering*, vol. 15, no. 3, pp. 351–364, 2020.
- [3] B. Mei, F. Xie, X.-J. Liu, Z. Xie, and H. Zhao, “A mobile hybrid robot and its accuracy issue in machining of large-scale structures,” *IEEE/ASME Transactions on Mechatronics*, vol. 29, no. 1, pp. 347–357, 2023.
- [4] K. Wang, H. Ju, Y. Yang, and Z. Guo, “An optimized permanent magnet brake mechanism in robot joints,” *IEEE Access*, vol. 9, pp. 18 278–18 286, 2021.
- [5] H. Dai Le, Q. H. Nguyen, S.-b. Choi *et al.*, “Design and experimental evaluation a novel magneto-rheological brake with tooth shaped rotor,” *Smart Materials and Structures*, vol. 31, no. 1, p. 015015, 2021.
- [6] D. Wang, G. Yang, Y. Luo, S. Fang, and T. Dong, “Optimal design and stability control of an automotive magnetorheological brake considering the temperature effect,” *Smart Materials and Structures*, vol. 32, no. 2, p. 025020, 2023.
- [7] A. De Luca, B. Siciliano, and L. Zollo, “Pd control with on-line gravity compensation for robots with elastic joints: Theory and experiments,” *automatica*, vol. 41, no. 10, pp. 1809–1819, 2005.
- [8] A. Calanca, R. Muradore, and P. Fiorini, “A review of algorithms for compliant control of stiff and fixed-compliance robots,” *IEEE/ASME transactions on mechatronics*, vol. 21, no. 2, pp. 613–624, 2015.
- [9] F. J. Abu-Dakka and M. Saveriano, “Variable impedance control and learning—a review,” *Frontiers in Robotics and AI*, vol. 7, p. 590681, 2020.
- [10] J. Cao, L. Qin, J. Liu, Q. Ren, C. C. Foo, H. Wang, H. P. Lee, and J. Zhu, “Untethered soft robot capable of stable locomotion using soft electrostatic actuators,” *Extreme Mechanics Letters*, vol. 21, pp. 9–16, 2018.
- [11] C. Tang, B. Du, S. Jiang, Q. Shao, X. Dong, X.-J. Liu, and H. Zhao, “A pipeline inspection robot for navigating tubular environments in the sub-centimeter scale,” *Science Robotics*, vol. 7, no. 66, p. eabm8597, 2022.
- [12] X. Yang, L. Chang, and N. O. Pérez-Arancibia, “An 88-milligram insect-scale autonomous crawling robot driven by a catalytic artificial muscle,” *Science Robotics*, vol. 5, no. 45, p. eaba0015, 2020.
- [13] X. An, Y. Cui, H. Sun, Q. Shao, and H. Zhao, “Active-cooling-in-the-loop controller design and implementation for an sma-driven soft robotic tentacle,” *ieee transactions on robotics*, vol. 39, no. 3, pp. 2325–2341, 2023.
- [14] E. Brown, N. Rodenberg, J. Amend, A. Mozeika, E. Steltz, M. R. Zakin, H. Lipson, and H. M. Jaeger, “Universal robotic gripper based on the jamming of granular material,” *Proceedings of the National Academy of Sciences*, vol. 107, no. 44, pp. 18 809–18 814, 2010.
- [15] F. Ilievski, A. D. Mazzeo, R. F. Shepherd, X. Chen, and G. Whitesides, “Soft robotics for chemists,” 2011.
- [16] D. Yang, M. Feng, J. Sun, Y. Wei, J. Zou, X. Zhu, and G. Gu, “Soft multifunctional bistable fabric mechanism for electronics-free autonomous robots,” *Science Advances*, vol. 11, no. 5, p. eads8734, 2025.
- [17] S. I. Rich, R. J. Wood, and C. Majidi, “Untethered soft robotics,” *Nature Electronics*, vol. 1, no. 2, pp. 102–112, 2018.
- [18] N. El-Atab, R. B. Mishra, F. Al-Modaf, L. Joharji, A. A. Alsharif, H. Alamoudi, M. Diaz, N. Qaiser, and M. M. Hussain, “Soft actuators for soft robotic applications: A review,” *Advanced Intelligent Systems*, vol. 2, no. 10, p. 2000128, 2020.

[19] T. Niino, T. Higuchi, S. Egawa, and N. Nishiguchi, "Dual excitation electrostatic stepping motor," *Electrical engineering in Japan*, vol. 119, no. 3, pp. 94–103, 1997.

[20] I. Choi, S. J. Yoon, and Y.-L. Park, "Linear electrostatic actuators with moiré-effect optical proprioceptive sensing and electroadhesive braking," *The International Journal of Robotics Research*, vol. 43, no. 5, pp. 646–664, 2024.

[21] G. Zhang, M. Osada, S. Yoshimoto, and A. Yamamoto, "A high performance muscle-like actuator using multi-layer electrostatic film motors," in *2022 IEEE 31st International Symposium on Industrial Electronics (ISIE)*. IEEE, 2022, pp. 1006–1011.

[22] T. Hosobata, A. Yamamoto, and T. Higuchi, "Transparent synchronous electrostatic actuator for long-stroke planar motion," *IEEE/ASME Transactions on Mechatronics*, vol. 20, no. 4, pp. 1765–1776, 2014.

[23] T. Hosobata, A. Yamamoto, and T. Higuchi, "2-dof synchronous electrostatic actuator with transparent electrodes arranged in checkerboard patterns," in *2013 IEEE/RSJ International Conference on Intelligent Robots and Systems*. IEEE, 2013, pp. 4919–4924.

[24] H. Wang and A. Yamamoto, "A thin electroadhesive inchworm climbing robot driven by an electrostatic film actuator for inspection in a narrow gap," in *2013 IEEE International Symposium on Safety, Security, and Rescue Robotics (SSRR)*. IEEE, 2013, pp. 1–6.

[25] H. Wang, A. Yamamoto, and T. Higuchi, "A crawler climbing robot integrating electroadhesion and electrostatic actuation," *International Journal of Advanced Robotic Systems*, vol. 11, no. 12, p. 191, 2014.

[26] H. Wang and A. Yamamoto, "Analyses and solutions for the buckling of thin and flexible electrostatic inchworm climbing robots," *IEEE Transactions on Robotics*, vol. 33, no. 4, pp. 889–900, 2017.

[27] R. Gassert, A. Yamamoto, D. Chapuis, L. Dovat, H. Bleuler, and E. Burdet, "Actuation methods for applications in mr environments," *Concepts in Magnetic Resonance Part B: Magnetic Resonance Engineering: An Educational Journal*, vol. 29, no. 4, pp. 191–209, 2006.

[28] M. Rajendra, A. Yamamoto, T. Oda, H. Kataoka, H. Yokota, R. Hineno, and T. Higuchi, "Motion generation in mr environment using electrostatic film motor for motion-triggered cine-mri," *IEEE/ASME Transactions on Mechatronics*, vol. 13, no. 3, pp. 278–285, 2008.

[29] W. Wang, D. Fan, R. Zhu, P. Wang, Y. Zhao, and H. Wang, "Modeling and optimization of electrostatic film actuators based on the method of moments," *Soft Robotics*, vol. 8, no. 6, pp. 651–661, 2021.

[30] Y. Qu, P. Wang, W. Wang, and H. Wang, "Analyses and optimization of electrostatic film actuators considering electrical breakdown," *IEEE Robotics and Automation Letters*, vol. 6, no. 2, pp. 1152–1159, 2021.

[31] G. Zhang and A. Yamamoto, "Position self-sensing for electrostatic motors under amplitude-modulated ac operation," *IEEE Transactions on Industrial Electronics*, vol. 71, no. 7, pp. 6809–6818, 2023.

[32] H. Wang, P. York, Y. Chen, S. Russo, T. Ranzani, C. Walsh, and R. J. Wood, "Biologically inspired electrostatic artificial muscles for insect-sized robots," *The International Journal of Robotics Research*, vol. 40, no. 6-7, pp. 895–922, 2021.

[33] T. Niino, S. Egawa, H. Kimura, and T. Higuchi, "Electrostatic artificial muscle: compact, high-power linear actuators with multiple-layer structures," in *Proceedings IEEE Micro Electro Mechanical Systems An Investigation of Micro Structures, Sensors, Actuators, Machines and Robotic Systems*. IEEE, 1994, pp. 130–135.

[34] A. Yamamoto, T. Niino, and T. Higuchi, "Modeling and identification of an electrostatic motor," *Precision engineering*, vol. 30, no. 1, pp. 104–113, 2006.

[35] Q. Xiong, X. Liang, D. Wei, H. Wang, R. Zhu, T. Wang, J. Mao, and H. Wang, "So-eaglove: Vr haptic glove rendering softness sensation with force-tunable electrostatic adhesive brakes," *IEEE Transactions on Robotics*, vol. 38, no. 6, pp. 3450–3462, 2022.

[36] A. Grabowski, P. Diez, and B. Schulze, "This is how pi does measuring - part ii," Physik Instrumente, Karlsruhe, Germany, Technical Report, Dec. 2020.